JOURNAL OF THE AMERICAN CHEMICAL SOCIETY
pubs.acs.org/JACS
Article

Redox-Induced Structural Reorganization Dictates Kinetics of Cobalt(III) Hydride Formation via Proton-Coupled Electron Transfer

Daniel A. Kurtz, Debanjan Dhar, Noémie Elgrishi, Banu Kandemir, Sean F. McWilliams, William C. Howland, Chun-Hsing Chen, and Jillian L. Dempsey*

Cite This: *J. Am. Chem. Soc.* 2021, 143, 3393−3406

Read Online

ACCESS | Metrics & More | Article Recommendations | SI Supporting Information

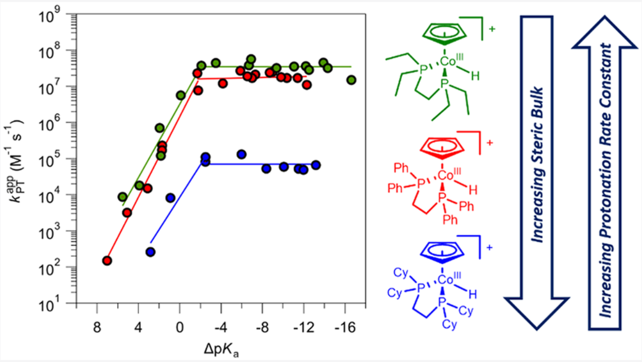

ABSTRACT: Two-electron, one-proton reactions of a family of $[CoCp(dxpe)(NCCH_3)]^{2+}$ complexes (Cp = cyclopentadienyl, dxpe = 1,2-bis(di(aryl/alkyl)phosphino)ethane) form the corresponding hydride species $[HCoCp(dxpe)]^+$ (dxpe = dppe (1,2-bis(diphenylphosphino)ethane), depe (1,2-bis(diethylphosphino)ethane), and dcpe (1,2-bis(dicyclohexylphosphino)ethane)) through a stepwise proton-coupled electron transfer process. For three $[CoCp(dxpe)(NCCH_3)]^{2+}$ complexes, peak shift analysis was employed to quantify apparent proton transfer rate constants from cyclic voltammograms recorded with acids ranging 22 pK_a units. The apparent proton transfer rate constants correlate with the strength of the proton source for weak acids, but these apparent proton transfer rate constants curiously plateau (k_{pl}) as the reaction becomes increasingly exergonic. The absolute apparent proton transfer rate constants across both these regions correlate with the steric bulk of the chelating diphosphine ligand, with bulkier ligands leading to slower kinetics ($k_{plateau,depe} = 3.5 \times 10^7$ M^{-1} s^{-1}, $k_{plateau,dppe} = 1.7 \times 10^7$ M^{-1} s^{-1}, $k_{plateau,dcpe} = 7.1 \times 10^4$ M^{-1} s^{-1}). Mechanistic studies were conducted to identify the cause of the aberrant $k_{PT}^{app}-\Delta pK_a$ trends. When deuterated acids are employed, deuterium incorporation in the Cp ring is observed, indicating protonation of the CoCp(dxpe) species to form the corresponding hydride proceeds via initial ligand protonation. Digital simulations of cyclic voltammograms show ligand loss accompanying initial reduction gates subsequent PCET activity at higher driving forces. Together, these experiments reveal the details of the reaction mechanism: reduction of the Co(III) species is followed by dissociation of the bound acetonitrile ligand, subsequent reduction of the unligated Co(II) species to form a Co(I) species is followed by protonation, which occurs at the Cp ring, followed by tautomerization to generate the stable Co(III)-hydride product $[HCoCp(dxpe)]^+$. Analysis as a function of chelating disphosphine ligand, solvent, and acid strength reveals that the ligand dissociation equilibrium is directly influenced by the steric bulk of the phosphine ligands and gates protonation, giving rise to the plateau of the apparent proton transfer rate constant with strong acids. The complexity of the reaction mechanism underpinning hydride formation, encompassing dynamic behavior of the entire ligand set, highlights the critical need to understand elementary reaction steps in proton-coupled electron transfer reactions.

■ INTRODUCTION

Just like a chain is only as strong as its weakest link, catalysis is only as fast as its slowest step(s). Consequently, understanding the nature of the rate-limiting step(s) in a catalytic cycle and the factors that influence it is crucial to improving the overall efficiency of a catalyst. In fuel-forming reactions such as hydrogen production or carbon dioxide reduction, the formation of transition metal−hydride bonds is a common elementary step that often has significant impact on the overall rates of product formation.[1−4] A transition metal hydride complex is often formed through a proton-coupled electron transfer process, via either a stepwise pathway (proton transfer followed by electron transfer, PT-ET, or vice versa, ET-PT) or a single concerted step (concerted proton−electron transfer, CPET).[4] While there have been numerous reports describing the application of electrochemical techniques to quantify the catalytic performance metrics of first-row transition metal hydrogen evolution catalysts,[3,5−8] limited work has focused on the specific parameters that influence the formation of metal hydride reaction intermediates. In this context, our group recently reported a systematic study on the effects of acid strength and structure on the observed rate constant of proton transfer (k_{PT}^{app}) of an electrochemically generated cobalt(I)

Received: November 16, 2020
Published: February 23, 2021

https://dx.doi.org/10.1021/jacs.0c11992

complex to form a stable cobalt(III) hydride complex from $[CoCp(dppe)(NCCH_3)][PF_6]_2$ (**1**, Cp = cyclopentadienyl, dppe = 1,2-bis(diphenylphosphino)ethane).[9] We observed a linear free-energy relationship for relatively weak acids and noted that sterically encumbered acids result in dramatically slower protonation when compared to acids with similar pK_a values and no steric bulk near the acidic proton. More intriguingly, we also observed a distinct plateau of k_{PT}^{app} values with stronger acids that extends over 14.5 kcal/mol of driving force for proton transfer. The second-order rate constants were 3 orders of magnitude lower than the calculated diffusion-limited rate constant. This plateau region alluded to underlying structural reorganization factors that limited the kinetics of hydride formation, as the pK_a of the added acid no longer affected the rate constant of proton transfer, but k_{PT}^{app} remained second order.

Aberrant rate constant−pK_a relationships such as the one highlighted above underscore the complexity of metal hydride formation reactions. Both structural reorganization and chemical steps such as ligand loss prior to formation of the active catalyst can dictate the kinetics associated with the formation of key intermediates in catalysis. This has previously been observed for the CO_2 reduction catalyst Re(bpy)-$(CO)_3Cl$. Upon reduction to $[Re(bpy)(CO)_3Cl]^{\bullet -}$, slow catalytic CO_2 reduction is initiated, but the observed kinetics are limited by slow chloride loss to allow for CO_2 coordination.[10] Similarly, the mechanism of oxidative addition of haloarenes to trialkylphosphine palladium(0) complexes, a key step in a suite of palladium-catalyzed cross-coupling reactions, was found to be crucially dependent on the nature of the halide, indicating that associative displacement of the ligand in the precatalyst is a key step in this multistep catalytic process.[11,12] Additionally, in examples of olefin polymerization using high-efficiency metallocene catalysts, backbone ligand reorganization has been proposed as the rate-limiting step of the reaction.[13]

Additional nuanced behavior has been detected in proton transfer reactions involving transition metal complexes supported by pentamethylcyclopentadienyl and other substituted cyclopentadienyl ligands. In several examples of low-valent complexes of cobalt,[14−16] rhodium,[17,18] and iron[19,20] with pentamethylcyclopentadienyl (Cp*) or indenyl ligands, initial protonation at the ring is preferential to protonation at the metal center, even when the metal hydride complex is thermodynamically more stable than the ring-protonated species. In some cases, the participation of the Cp* ligand in the initial protonation event and subsequent tautomerization to form the metal hydride complex is proposed to be crucial for hydrogen evolution catalysis.[21] This observed proton relay reactivity is analogous to that observed with intentionally placed amine-based pendant bases in nickel-based hydrogen evolution electrocatalysts.[2] Peters and co-workers have reported that protonation of Cp* rings may be important for nitrogen reduction to NH_3 where $[Cp^*Co(\eta^4\text{-}C_5Me_5H)]^+$ is a highly reactive PCET donor. Blakemore and co-workers have shown that accompanying ligands can dramatically affect whether Cp*-rhodium-based complexes are protonated or not.[22−24] The observation of kinetically facile ligand protonation over more sluggish metal protonation is best contextualized in the pioneering works of Norton and Pearson. Protonation/deprotonation reactions involving metal complexes are noted to be more similar to those involving carbon acids than oxygen- or nitrogen-based acids.[25−29] Large geometric and structural rearrangements can occur during acid/base reactions involving metal complexes, imparting substantial reorganization energies that attenuate rate constants of these reactions.

In this work, we interrogate the PCET reaction kinetics for a series of three cobalt complexes with cyclopentadienyl and chelating bisphosphine ligands that react via proton-coupled electron transfer to form stable metal hydride complexes. While not active catalysts, these model complexes enable the PCET process associated with hydride formation to be decoupled from catalyst turnover, and their sterics and electronics are readily tunable through ligand substitution. Here, by varying the identity of the phosphine substituents, the steric bulk of the chelating bisphosphine ligand (generically termed dxpe) was systematically perturbed, enabling us to interrogate the role of structural changes in governing the observed kinetics of hydride formation and gain deep insight into the reaction pathway through which the hydride complexes form. All three $[CoCp(dxpe)(NCCH_3)]^{2+}$ complexes react via a stepwise electron transfer−electron transfer−proton transfer pathway to form the corresponding [HCoCp-(dxpe)]$^+$ and exhibit a linear free-energy relationship (LFER) between the apparent proton transfer rate constant (k_{PT}^{app}) and proton source pK_a at low driving force. As the proton transfer process becomes mildly exergonic ($\Delta pK_a \approx -2$), k_{PT}^{app} becomes driving force-independent. The phosphine substituents indeed have a significant impact on absolute magnitude of the observed proton transfer kinetics across both these regions, but the general observation of a LFER and a plateau region in the Brønsted plots remains invariant.

Reaction kinetics quantified in noncoordinating solvents reveal that ligand loss accompanying initial reduction gates subsequent PCET activity at higher driving forces. Comprehensive kinetics simulations incorporating this elementary step and its independently measured rate constants and equilibrium constants rationalize the aberrant $k_{PT}^{app}-\Delta pK_a$ trends. The ligand dissociation process—which is accompanied by substantial geometric rearrangement—directly correlates to the steric bulk of the bisphosphine ligand. Further, we unveil evidence that protonation proceeds through the Cp ligand, followed by tautomerization to form the hydride species, rather than directly to the metal center, indicating a substantial kinetic barrier to direct metal protonation. These data reveal a reaction mechanism of hydride formation that illustrates the potential for latent complexity in PCET reactions as the cobalt complex negotiates a series of elementary reaction steps that implicate the dynamic behavior of the entire ligand set despite both the proton and electron ultimately residing on the metal center. Ultimately, these conclusions underscore how deceptively simple reaction schemes can veil complex mechanisms and showcase how mechanistic studies can elucidate the key roles both metal and ligand play in mediating substrate transformations.

■ RESULTS AND DISCUSSION

Synthesis and Characterization of the [CoCp(dxpe)-$(NCCH_3)]^{2+}$ Complexes. Three cobalt(III) complexes with bis(phosphino)ethane ligands generically termed dxpe were synthesized through routes described previously involving a common $[CoCp(SMe_2)_3][PF_6]_2$ precursor (**1**−**3**, Scheme 1).[30] In comparison to the previously studied complex $[CoCp(dppe)(NCCH_3)][PF_6]_2$ (**1**), [CoCp(depe)-$(NCCH_3)][PF_6]_2$ (**2**, depe = 1,2-bis(diethylphosphino)-

Scheme 1. Synthetic Routes to $[CoCp(dxpe)(NCCH_3)][PF_6]_2$ and $[HCoCp(dxpe)][PF_6]$ Complexes.

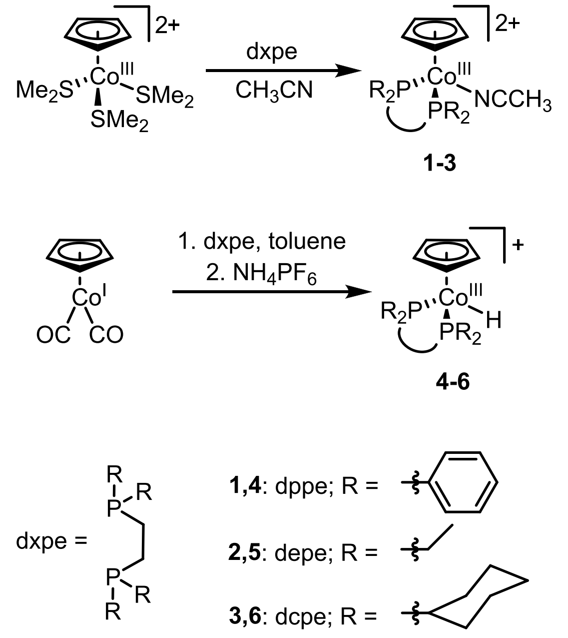

ethane) has a less sterically bulky phosphine ligand, while $[CoCp(dcpe)(NCCH_3)][PF_6]_2$ (**3**, dcpe = 1,2-bis(dicyclohexylphosphino)ethane) is coordinated by a sterically encumbered phosphine. The cobalt(III) hydride complexes (**4**–**6**) were prepared and isolated by first combining $CoCp(CO)_2$ and dxpe in toluene and heating to generate the corresponding cobalt(I) complexes CoCp(dxpe), followed immediately by protonation with $[NH_4][PF_6]$. All complexes were characterized using multinuclear NMR spectroscopy (Figures S1–S16) and UV–visible absorbance spectroscopy (Figures S17 and S18). Single crystals of the two new hydride complexes **5** and **6** were grown and characterized by single-crystal X-ray diffraction (SC-XRD) analysis (Figures S73 and S74, bond distances and bond angles in Tables S10, S11, S13, and S14). The hydride ligand for **5** was placed in its ideal position and was first refined using individual relative isotropic displacement parameters and later in fixed position to reduce the number of parameters, and a Co–H bond length of 1.413 Å was determined without esds. The hydride ligand in **6** was obtained from the Fourier difference map, its position was refined, and a Co–H bond length of 1.35(5) Å was obtained. While the SC-XRD method cannot yield accurate hydrogen positions,[31] the bond lengths are broadly in line with other reported metal hydride bond distances, and the SC-XRD data support the overall connectivity shown in Scheme 1.[32]

To probe the effects of the electronic perturbations caused by altering the supporting bisphosphine ligand, the pK_a values of hydrides **5** and **6** were quantified via spectrophotometric titration (Figures S19 and S20) and compared to the previously reported pK_a value of **4**.[9] The pK_a values of **5** and **6**, 23.6 and 22.6, respectively, indicate complexes with more strongly donating alkyl phosphines are significantly more basic than the previously reported aryl-substituted **4** (pK_a = 18.4).[9] Notably, these electronic effects are also manifested in the hydride resonance in the ^{1}H NMR spectrum of each complex; the alkyl phosphine complexes exhibit hydride resonances more upfield (−16.7 ppm for **5** and −16.5 ppm for **6**) than the aryl phosphine complex (−15.3 ppm for **4**).

Electrochemical Analysis in the Absence of Acid. To probe the effects of the ligand electronics on the metal-centered redox events, cyclic voltammograms were recorded for complexes **1**–**3** in 0.25 M $[Bu_4N][PF_6]$ acetonitrile solution. Voltammograms of **2** and **3** exhibit two reversible waves assigned to Co(III/II) and Co(II/I) couples, similar to that reported previously for **1** (Figure 1, Table 1).[9] For **2**, both the Co(III/II) (−0.71 V vs $Fc^{+/0}$) and Co(II/I) (−1.21 V vs $Fc^{+/0}$) couples are shifted to more negative potentials compared to **1** (−0.51 and −0.93 V vs $Fc^{+/0}$, respectively), as expected for the stronger alkyl phosphine donor ligand in comparison to the arylphosphine.[33] While the Co(II/I) couple of the cyclohexyl-substituted phosphine derivative **3** ($E_{1/2}$ = −1.25 V vs $Fc^{+/0}$) is similarly shifted to more negative potentials in comparison to **1**, the Co(III/II) couple appears at a significantly more positive potential ($E_{1/2}$ = −0.39 V vs $Fc^{+/0}$). Additionally, when voltammograms of the analyte solution are recorded at various time delays (0–4.5 h) after dissolution in CH_3CN under an N_2 atmosphere, the Co(III/II) wave for **3** broadens and assumes a more quasi-reversible form with ΔE > 57 mV (Figure S21). This anomalous behavior is discussed below. The diffusion coefficients and heterogeneous electron transfer rate constants for complexes **2** and **3** are

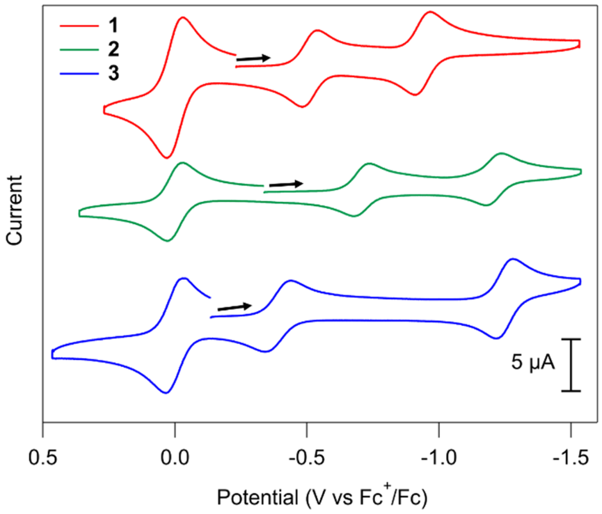

Figure 1. Cyclic voltammograms of **1**–**3** (1 mM) recording in 0.25 M $[NBu_4][PF_6]$ CH_3CN at υ = 100 mV s^{-1}. The internal standard Fc is present in each scan, and all voltammograms are referenced the Fc^+/Fc redox couple.

Table 1. Electrochemical Properties of 1–3 in CH_3CN

	potential (V vs Fc^+/Fc)		diffusion coefficient (D, cm^2 s^{-1})		k_s (cm s^{-1})	
complex (ligand)	Co(III/II)	Co(II/I)	Co(III/II)	Co(II/I)	Co(III/II)	Co(II/I)
1 (dppe)	−0.51[a]	−0.93[a]	3.4×10^{-6}	5.2×10^{-6}	0.051	0.11
2 (depe)	−0.71[a]	−1.21[a]	4.4×10^{-6}	6.7×10^{-6}	0.022	0.36
3 (dcpe)	−0.39[b]	−1.25[a]		7.0×10^{-6}		0.19

[a] $E°'$. [b] $E_{1/2}$, apparent potential, shifted from $E°$ by ligand equilibrium.

Scheme 2. Solvent Loss upon One-Electron Reduction of the Cobalt(III) Complexes

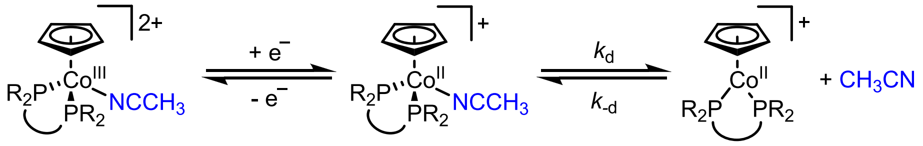

Scheme 3. Net Electrochemical Reaction Scheme in the Presence of Acid

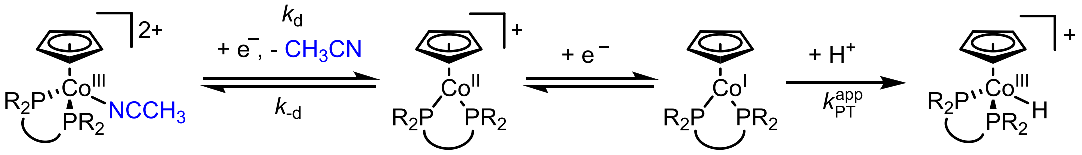

similar to those reported previously for **1** (Figures S22−S25, Table 1).[9]

Interrogating CH_3CN Ligand Loss. For **1**, reduction to the Co(II) species leads to a concomitant dissociation of the bound CH_3CN (Scheme 2), which is detected by a loss of reversibility for the Co(III/II) couple in voltammograms recorded in a noncoordinating solvent such as CH_2Cl_2.[9] While previous experiments using **1** were performed in CH_2Cl_2, the analogous measurement of **2** in CH_2Cl_2 was precluded by noticeable reactivity, presumably with the solvent (Figure S26). Therefore, ligand loss was studied in another noncoordinating solvent (1,2-difluorobenzene, DFB), compatible with both **1** and **2**. Using the scan rate-dependent peak shift of $E_{p,c}$ (eq 1, where R, T, and F are the gas constant, temperature, and Faraday's constant, respectively),[34] the rate constant for ligand loss (k_d) for **2** in DFB was found ($k_d = 6.8 \times 10^4$ s^{-1}, Figure S27). For **1**, a k_d value of 1.8×10^4 s^{-1} in DFB was determined (Figure S28). Notably, the rate constant for **1** is ∼3 orders of magnitude smaller in DFB compared to that in CH_2Cl_2 ($k_d = 4 \times 10^7$ s^{-1}). Comparison of the ethyl- and phenyl- substituted complexes indicates that CH_3CN dissociation is ∼4 times faster for **2** than **1** in DFB.

$$E_{pc} = E_{1/2} - \frac{RT}{F}(0.78) + \frac{RT}{2F}\ln\left(\frac{k_d RT}{Fv}\right) \quad (1)$$

For both **1** and **2**, titration of CH_3CN to the analyte solution results in regaining of reversibility of the Co(III/II) feature, indicating that CH_3CN loss is reversible (Figure S29). We define K_{eq} by eq 2, noting that for practical purposes the equilibrium constant has units of M.[35,36] With this expression for K_{eq}, the apparent $E_{1/2}$ ($E^{0'}$) relates to the true $E_{1/2}$ of the Co(III/II) couple through eq 3:

$$K_{eq} = \frac{[\mathrm{Co(II)}][\mathrm{CH_3CN}]}{[\mathrm{Co(II)-NCCH_3}]} = \frac{k_d}{k_{-d}} \quad (2)$$

$$E^{0'} = E_{1/2} + \frac{RT}{F}\ln\left(1 + \frac{K_{eq}}{[\mathrm{CH_3CN}]}\right) \quad (3)$$

For **1**, analysis of the $E_{1/2}$ peak shift in DFB as a function of 1/[CH_3CN] (eq 3) yields an equilibrium constant value for solvent dissociation (K_{eq}) of 25 M (Figure S30), which is slightly lower than the previously reported value in CH_2Cl_2 (K_{eq} = 76 M).[9] Similar analysis for **2** in DFB yields a K_{eq} value of 50 M (Figure S31). These results indicate that this equilibrium constant for solvent dissociation is dependent on both the nature of the bisphosphine ligand and the solvent.

The electrochemical behavior of **3** in both DFB and CH_2Cl_2 is starkly different from that observed for **1** and **2**. The Co(III/II) feature is irreversible as anticipated (Figure S29), but it appears at a substantially more negative potential ($E_{p,c} \approx -0.56$ V vs Fc$^{+/0}$ at 200 mV s^{-1}) when compared to that in CH_3CN ($E_{1/2} = -0.39$ V vs Fc$^{+/0}$). This observation contradicts the shift to more positive potentials that would be consistent with the EC reactivity resulting from coordinated CH_3CN loss upon one-electron reduction. Further, titration of CH_3CN into a DFB solution of **3** does not result in enhanced reversibility of the Co(III/II) voltammetric feature, indicating that CH_3CN loss from Co(II) is irreversible for **3** (Figure S29). We hypothesize that for **3** the bulky dcpe ligand places CH_3CN coordination in equilibrium in the Co(III) oxidation state ($[\mathrm{CoCp(dcpe)(NCCH_3)}]^{2+} \rightleftharpoons [\mathrm{CoCp(dcpe)}]^{2+} + \mathrm{CH_3CN}$), consistent with speciation of related cobalt complexes.[37] Slow CH_3CN coordination/dissociation explains the observed broadening of the Co(III/II) redox feature in neat CH_3CN over time, as described above. In order to explore this hypothesis, we compared computationally predicted free-energy changes associated with dissociation of CH_3CN in both the Co(III) and Co(II) oxidation states for complexes **1**−**3** (Table S1). These data show that while the loss of CH_3CN from Co(III) is significantly uphill for **1** and **2** (calculated ΔG values of +19.6 and +27.1 kcal/mol, respectively), this reaction is uphill only by 6.4 kcal/mol for **3**, and thus at room temperature $[\mathrm{CoCp(dcpe)(NCCH_3)}]^{2+}$ is in equilibrium with $[\mathrm{CoCp(dcpe)}]^{2+}$ ($K \approx 2 \times 10^{-5}$ M). In contrast, the corresponding reactions involving CH_3CN loss in the Co(II) oxidation state are all predicted to be exergonic, with a substantially larger driving force for **3** (−15.4 kcal/mol) than **1** and **2** (−5.9 and −6.5 kcal/mol, respectively). Unfortunately, owing to this complex ligation equilibrium of **3**, we are unable to determine k_d for **3** using eq 1, as we do not know the true $E_{1/2}$ for **3** in the absence of any CH_3CN loss.

Voltammetric Responses in the Presence of a Proton Source. When cyclic voltammograms of **2** and **3** in CH_3CN are recorded in the presence of added acid, the Co(II/I) redox feature becomes irreversible and the cathodic peak potential shifts more positive, as was previously observed for **1**.[9] The Co(II/I) peak position evolves as a function of scan rate, consistent with an EC process in which an irreversible chemical (C) step follows a fast electron transfer (E) (Scheme 3).

Consistent with previously reported reactivity of **1**,[9] we assign the chemical step following reduction of Co(II) as protonation of the Co(I) species to form the corresponding Co(III) hydride complex. The peak potential shifts as a

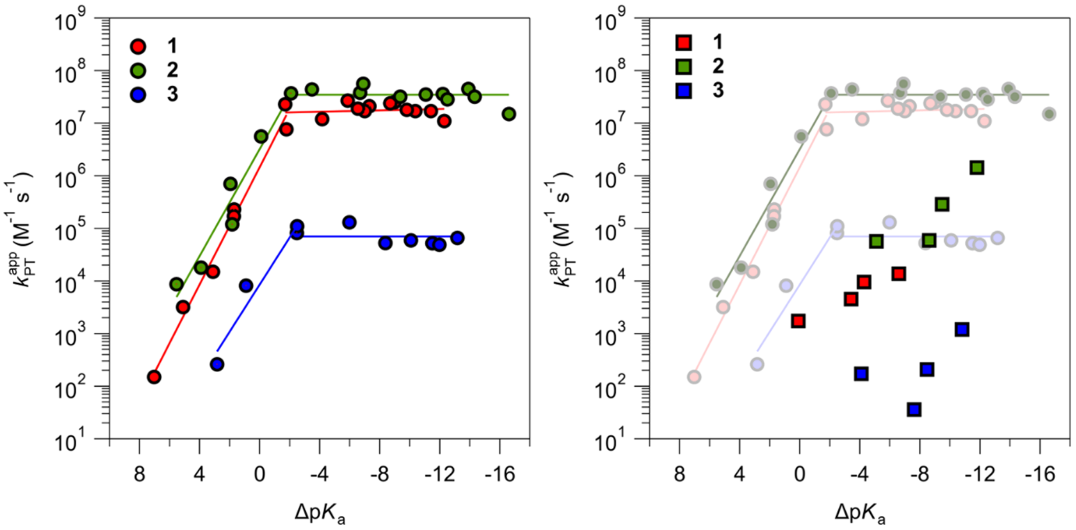

Figure 2. Brønsted plots for the apparent proton transfer rate constant k_{PT}^{app} of Co(I) species using (left) nonbulky acids and (right) highlighting sterically encumbered acids.

function of both acid concentration ([HA]) and scan rate (v) according to

$$E_{pc} = E_{1/2} - \frac{RT}{F}(0.78) + \frac{RT}{2F}\ln\left(\frac{k_{PT}^{app}[HA]RT}{Fv}\right) \tag{4}$$

where $E_{1/2}$ is the half-wave potential of the one-electron reversible electrochemical event in the absence of a coupled chemical step, and k_{PT}^{app} the apparent rate constant for protonation. The evolution of the peak potential with acid concentration or scan rate allows ready determination of k_{PT}^{app}.[34]

Apparent proton transfer rate constants were determined for **2** and **3** for a range of acids spanning 22 pK_a units in acetonitrile (Figure 2, Tables S2 and S3, illustrative data in Figures S33−S58). Rate constants are unique for each acid−cobalt complex combination. These differences are anticipated, as the driving force for proton transfer is quantified by the difference in pK_a values of the hydride complex and the acid. To account for this, Brønsted plots are presented as k_{PT}^{app} vs ΔpK_a, where ΔpK_a is the difference between the pK_a of the added acid and the pK_a of the Co(III) hydride species $[HCoCp(dxpe)]^+$ in order to facilitate comparison across the three different complexes studied (Figure 2). The three Brønsted plots are similar in shape, each with three distinct regions: (1) a linear free-energy relationship region where k_{PT}^{app} varies with ΔpK_a, (2) a region where proton transfer rate constants plateau at mildly exergonic proton transfers (starting at ∼ΔpK_a = −2) with a “plateau rate constant” value ($k_{plateau}$), and (3) data points that align with neither region 1 or 2, but share a commonality that the acids have steric bulk about the acidic proton. The LFER region in each plot has a similar Brønsted slope (α), with no significant trend in α values across the series: $\alpha_1 = 0.55$, $\alpha_2 = 0.51$, and $\alpha_3 = 0.45$. These α values are similar to those reported for protonation to form other transition metal hydride complexes.[29] Across the three complexes, the absolute rate constants are consistently highest for the depe ligand, followed by the dppe and the dcpe ligand, qualitatively correlating with the steric bulk of the ligand. Consistent with previous observations for **1**, protonation reactions of **2** and **3** with acids with steric bulk around the acidic proton are slower than expected based on the acid pK_a. Using a series of *para*-substituted 2,6-dimethylpyridinium acids, we observe different linear free-energy relationships within the group of bulky acids for each complex with a lower LFER slope ($\alpha \approx 0.1{-}0.2$), albeit with fewer data points than the nonbulky LFER regions. Additionally, for k_{PT}^{app} values that are too low (in this case, when $E_{p,c} < E_{1/2}$), the peak-shift analysis breaks down, and thus for complex **3** with bulky acids, the data are not reliable. Thus, we refrain from quantitative conclusions from these bulky acid data.

For all complexes, second-order k_{PT}^{app} values become independent of acid strength when the difference between the pK_a of the hydride complex and the acid exceeds ca. 3 pK_a units, leading to a distinct plateau in the Brønsted plot. Like the LFER region, the maximum proton transfer rate constant defining this plateau ($k_{plateau}$) qualitatively correlates with the steric bulk of the phosphine substituent; the ethyl-substituted phosphine ligand (3.5×10^7 M^{-1} s^{-1}) has the largest plateau rate constant, followed by the phenyl-substituted ligand (1.7×10^7 M^{-1} s^{-1}) and the cyclohexyl-substituted ligand (7.1×10^4 M^{-1} s^{-1}).

To better quantify the observed correlations between k_{PT}^{app} values and steric bulk of **1**, **2**, and **3** in the LFER and plateau regions, we sought to gain additional quantification of how ligand sterics influence kinetics of metal protonation. Norton has previously described the intrinsic barrier to protonation of reduced metal complexes to form metal hydride complexes.[25,38−40] These intrinsic barriers are well described by reorganization energies, which can be extracted from self-exchange rate constants for proton transfer (k_{self}). While ^1H NMR techniques such as variable-temperature NMR and line broadening have previously been used to determine k_{self} values,[29] no appreciable amount of broadening was observed in the cyclopentadienyl resonances of mixtures of the studied cobalt(III) hydride and cobalt(I) complexes up to 70 °C, indicating the exchange was slower than could be quantified by these tools. Two-dimensional exchange spectroscopy (2D-EXSY) ^1H NMR can measure rate constants on slower time scales (0.01−100 s^{-1}), although this technique has seen limited application to measure rate constants for atom transfer reactions.[41,42] For the self-exchange reaction between the cobalt(III) hydride and its conjugate base, kinetic information can be obtained using appropriate mixing times and the

https://dx.doi.org/10.1021/jacs.0c11992
J. Am. Chem. Soc. 2021, 143, 3393−3406

relative integrals of the off-diagonal EXSY peaks in the 2D NMR. To minimize the effects of longitudinal relaxation, which are rather large in these cobalt complexes ($T_1 < 0.3$ s), the smallest mixing time that gave appreciable off-diagonal EXSY peaks was used, typically 50−100 ms.[41] Following these protocols, k_{self} values were quantified for $[HCoCp(dppe)]^+$/CoCp(dppe) and $[HCoCp(depe)]^+$/CoCp(depe) in CD_3CN/C_6D_6 mixtures (1:1, for solubility, Figures S59 and S60). As predicted, the k_{self} value for the ethyl-substituted complexes ($k_{self\text{-}2}$ = 61 M^{-1} s^{-1}) was higher than that of the bulkier phenyl-substituted complexes ($k_{self\text{-}1}$ = 3.1 M^{-1} s^{-1}), supporting the conclusion that k_{PT}^{app} values are influenced by steric bulk. Extremely low solubility of CoCp(dcpe) thwarted attempts to obtain the value of $k_{self\text{-}3}$ using this method.

Understanding the Plateau Region in the Brønsted Plots. While k_{self} values provide support and quantification for the observation that the absolute k_{PT}^{app} values trend with ligand sterics in the LFER region and the plateau region, they do not provide a rationale for the observation that k_{PT}^{app} becomes independent of the acid strength when the proton transfer reaction becomes mildly exergonic. To understand this abrupt plateau of rate constants, we considered how either a change in mechanism or a change in rate law might give rise to driving force-independent k_{PT}^{app} values.

Protonation of Co(I) Proceeds Indirectly via Ligand Protonation. Preferential protonation of pentamethylcyclopentadienyl and other cyclopentadienyl-based ligands over a metal ion has previously been reported as discussed above.[14−17] We hypothesized that a change in mechanism—protonation at the metal center with weaker acids and protonation at the cyclopentadienyl ligand with stronger acids followed by a intramolecular proton transfer to the metal center—could explain the two distinct regimes observed in the Brønsted plots. To evaluate whether protonation proceeded through the cyclopentadienyl ring, we treated CoCp(dppe) with 1 equiv of d_3-anilinium (pK_a = 10.41). If the metal was directly protonated, deuterium incorporation would be observed exclusively in the metal hydride resonance. However, deuterium incorporation in both the Cp ring and the hydride was observed in the ^{2}H NMR spectrum of the reaction product, indicating that protonation proceeds with participation of the cyclopentadienyl ligand (Figure S61). The observation of both Cp-d_1 and DCo(III) suggests either protonation is unselective for the endo vs exo positions or the two-step protonation is reversible. When the same reaction was carried out using 10 equiv of the weaker acid CD_3COOD (pK_a = 23.51), deuterium incorporation was again observed in both the cyclopentadienyl and hydride resonances. These data indicate that protonation of the CoCp(dppe) to form $[HCoCp(dppe)]^+$ proceeds via initial ligand protonation in both the LFER and plateau regions, followed by intramolecular proton transfer. DFT calculations indicate that both steps are substantially exergonic (−17.1 and−18.6 kcal mol^{-1}, respectively; Scheme S2 and Table S8, Supporting Information). Similar relative energetics are computed for **2** and **3**, and we thus expect this mechanism is operative for these complexes as well. While these data do not support the hypothesis that a change in initial protonation site is responsible for the abrupt change in k_{PT}^{app}−pK_a relationships observed at the junction of the LFER and plateau regions, they do suggest a large kinetic barrier for direct, metal-centered protonation of CoCp(dxpe), a finding that has substantial ramifications for understanding PCET reactions that form metal hydride complexes.

To contextualize the $[HCoCp(dxpe)]^+$/CoCp(dxpe) self-exchange rate constants described above with this mechanistic finding, we sought to assess whether self-exchange proceeds via direct metal-to-metal proton transfer or via an initial ligand protonation. When the deuteride reagent $NaBD_4$ was added to $[CoCp(dppe)(NCCH_3)]^{2+}$, $[DCoCp(dppe)]^+$ was observed as the exclusive product, with no deuterium incorporation in the Cp ring detected (Figure S62). This result indicates that Cp protons and the hydride proton do not exchange with each other. However, when equimolar amounts of CoCp(dppe) and $[DCoCp(dppe)]^+$ were mixed, deuterium incorporation in the Cp ring was observed (Figure S62), indicating that the proton transfer self-exchange reaction proceeds via a two-step process through initial Cp protonation followed by tautomerization to yield the $[DCoCp(dppe)]^+$. These data inform us that the self-exchange proton transfer rate constants obtained via EXSY are an apparent self-exchange rate constant and are *not* an accurate measure of the direct proton transfer barrier.

While the deuterium incorporation data do not support a change in the overall mechanism between the LFER and plateau regions, we recognized that a change in rate-limiting step(s) as a function of driving force is possible, given the indirect, two-step hydride formation process elucidated. We first hypothesized that in the LFER region (endergonic to mildly exergonic proton transfer), the observed reaction kinetics would be dominated by intermolecular proton transfer from the acid to the cyclopentadienyl ring of CoCp(dxpe), while in the plateau region (significantly exergonic proton transfer) tautomerization from the $[Co(CpH)(dxpe)]^+$ to the $[HCoCp(dxpe)]^+$ would control the rate law. If the rate of tautomerization dictated the reaction kinetics, the acid pK_a independence of k_{PT}^{app} reflects the intrinsic barrier associated with this intramolecular tautomerization. However, this model is not consistent with the observation of an acid concentration-dependent peak shift in the plateau region.[9]

Interrogation of the Rate Law. We next evaluated whether the rate law differs between the LFER region and the plateau region by quantifying the kinetic isotope effect (KIE) of k_{PT}^{app}. k_{PT}^{app} values were quantified with proteo (k_H) and deuterated (k_D) acids for two proton sources, one with a pK_a value in the LFER region (acetic acid, pK_a = 23.51) and a second in the plateau region of the Brønsted plot (anilinium, pK_a = 10.41), to compare KIE values of **1** in CH_3CN. A normal, primary KIE was observed for acetic acid (k_H/k_D = 4.5, Figure S63), indicating that proton transfer is involved in the rate-limiting step(s) in the LFER, while an inverse KIE (k_H/k_D = 0.75, Figures S64 and S65) was quantified for anilinium, suggesting that the rate-controlling process is different with stronger acids that fall in the plateau region. Inverse KIE values often indicate a pre-equilibrium process prior to a rate-limiting step involving the proton transfer. For instance, the reductive elimination of RH from the tungsten hydride complex $[Me_2Si(C_5Me_4)_2]$W(R)H has an inverse KIE, attributed to an inverse equilibrium isotope effect in the multistep reaction and not due to kinetic differences in a single step.[43]

In studies interrogating the formation of $[HCoCp(dxpe)]^+$ described in this work, the Co(I) synthon CoCp(dxpe) is accessed *in situ* via the two-electron reduction of the $[CoCp(dxpe)(NCCH_3)]^{2+}$ precursor (Scheme 3). The reduction of the Co(III) species to Co(II) is accompanied by a concomitant dissociation of the coordinated acetonitrile ligand for **1** and **2** (see above); subsequent electron transfer occurs to the unligated Co(II) complex. The reduction-induced ligand

Scheme 4. Overall Mechanism for the Electrochemical Reaction

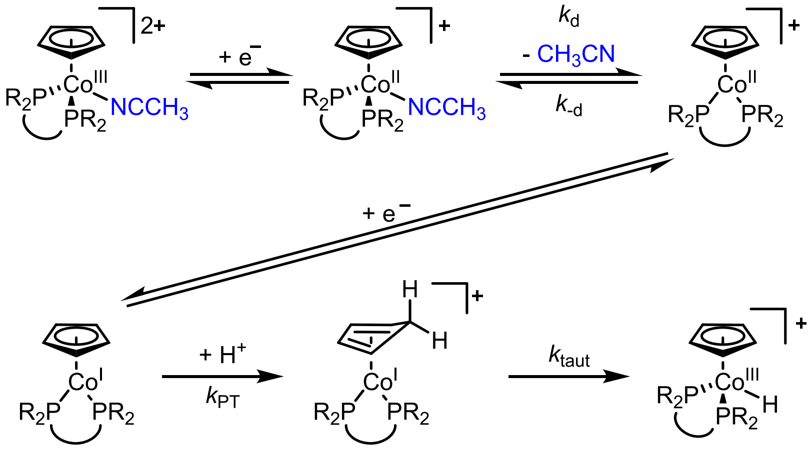

dissociation differs for the cyclohexyl-substituted complex **3**, as coordination of CH_3CN to the Co(III) species is under equilibrium for this complex (see above). Whereas the quantification of k_{PT}^{app} discussed above is based on a simple EC model (eq 4) and assumes the ligand dissociation does not influence proton transfer kinetics, KIE data suggest ligand dissociation from the electrochemically generated Co(II) may play a crucial role in the observed kinetics of protonation. To test this hypothesis, we performed digital simulations of cyclic voltammograms based on an $EC_1EC_2C_3$ reaction mechanism that includes CH_3CN ligand dissociation from the Co(II) species (C_1) and initial protonation on the Cp ring of the Co(II) species (C_2), followed by a tautomerization step (k_{taut}) that yields the Co(III) hydride (C_3) (Scheme 4, detailed expressions included in the Supporting Information).

Digital simulations of cyclic voltammograms were carried out for the $EC_1EC_2C_3$ PCET reactivity of **1** in bulk CH_3CN using the reaction mechanism depicted in Scheme 4 and experimentally determined values of diffusion coefficients and heterogeneous rate constants (Table 1). We are unable to experimentally determine the rate constant (k_d) and equilibrium constant (K_{eq}) for CH_3CN dissociation in neat CH_3CN (see above), and therefore approximated those values using the parameters quantified in CH_2Cl_2 ($k_d = 4 \times 10^7$ s^{-1} and $K_{eq} = 76$ M) for this qualitative model.[9] The final step of the intramolecular proton tautomerization is assumed to be irreversible. The specific rate constant for tautomerization (k_{taut}) was found not to influence the simulations (10^4–10^{14} s^{-1}) and generally set to 1×10^{14} s^{-1} in all simulations. Initial simulations were conducted at a fixed scan rate (200 mV s^{-1}) for 0.5 mM **1** and 50 mM acid; the driving force and the rate constant for protonation of CoCp(dppe) were varied by changing the pK_a of the acid (Figure S66).

First, cyclic voltammograms were simulated for acids aligned with the LFER region of the Brønsted plots ($8 \geq \Delta pK_a \geq -2$). On the basis of the slope of the Brønsted plot in the LFER region (~0.5), we assume that a 2-unit decrease in the ΔpK_a is accompanied by a 10-fold increase in k_{PT} (10^2 M^{-1} s$^{-1} \leq k_{PT} \leq 10^7$ M^{-1} s^{-1}). In these simulations, the $E_{p,c}$ value of the Co(II/I) reduction wave shifts positive as the input value of k_{PT} is increased, consistent with experimental data which has been interpreted by an increase in the apparent proton transfer rate constant with stronger acids (Figure 3). In this region, simulations predict that $E_{p,c}$ is dependent on the scan rate (Figure S67) and acid concentration (Figure S68), in agreement with experimental observations.[9] Importantly, when k_{PT}^{app} values are determined from the $E_{p,c}$ values of the simulated data and eq 4, a reasonable agreement between the input k_{PT} values and the calculated k_{PT}^{app} is found (e.g., when the k_{PT} input values are 100 and 1000 M^{-1} s^{-1}, the corresponding k_{PT}^{app} values are 98 and 640 M^{-1} s^{-1}, respectively). This indicates that in the LFER region the rate constants (k_{PT}^{app}) obtained using the EC peak shift analysis discussed above are indeed representative of the intrinsic proton transfer rate constant k_{PT}. On this basis, we attribute the differences observed in k_{PT}^{app} for **1**, **2**, and **3** in the LFER region—where k_{PT}^{app} values trend with the bulk of the ligand—to differences in the steric profile of the dxpe ligands. Steric bulk around the cobalt center dictates the approach of molecular acids to the nucleophilic CoCp(dxpe) in the bimolecular proton transfer process, much like steric bulk around the acidic proton of the acid does (see above).

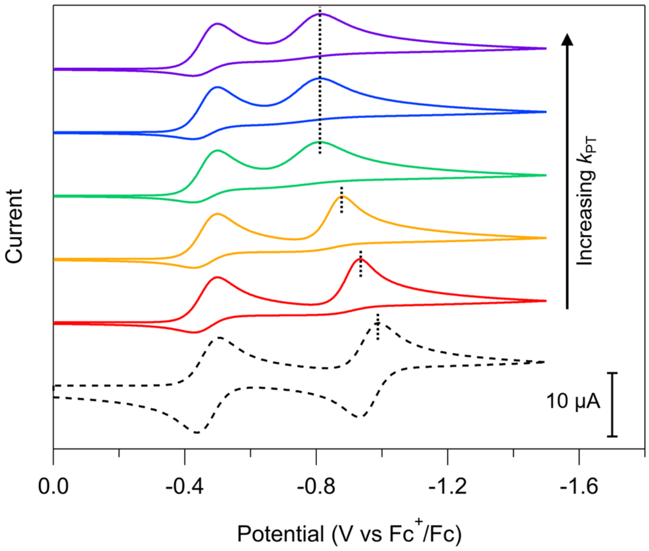

Figure 3. Simulated cyclic voltammograms for **1** (0.5 mM) in CH_3CN in the presence of 50 mM acid at 200 mV s^{-1} with varying input k_{PT} values: 1×10^4 M^{-1} s^{-1} (red), 1×10^6 M^{-1} s^{-1} (yellow), 1×10^9 M^{-1} s^{-1} (green), 5×10^9 M^{-1} s^{-1} (blue), and 1×10^{10} M^{-1} s^{-1} (purple). The dashed black trace is the simulated voltammogram in the absence of any added acid. Simulations are carried out using the reaction scheme and parameters listed in Scheme S1.

https://dx.doi.org/10.1021/jacs.0c11992
J. Am. Chem. Soc. 2021, 143, 3393−3406

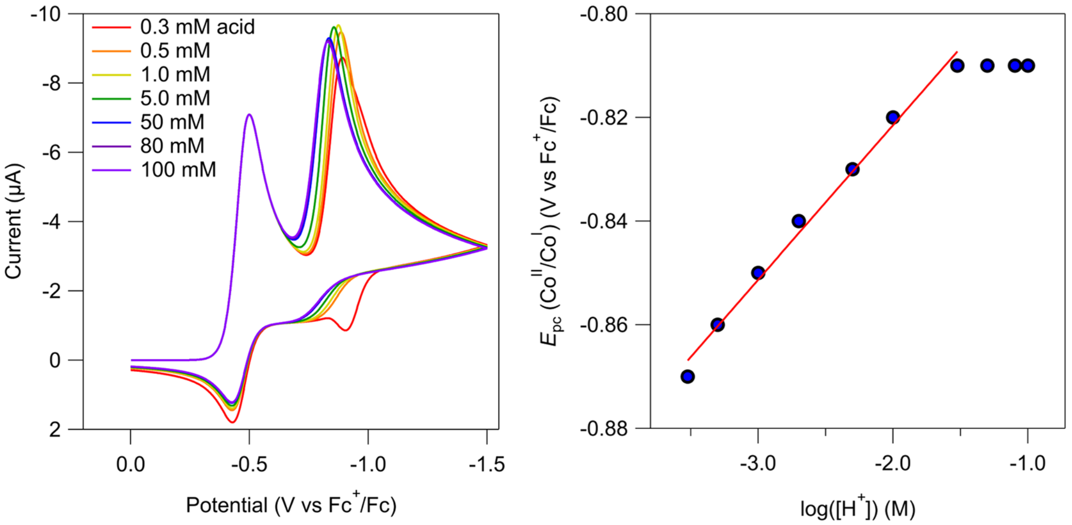

Figure 4. (Left) Simulated voltammograms for 0.5 mM **1** with varying amounts of acid at 200 mV s^{-1}, using a k_{PT} value of 1×10^9 M^{-1} s^{-1}. (Right) Variation of $E_{p,c}$ in simulated voltammograms with log(acid concentration) input. The red line is a linear fit (R^2 = 0.9989) with a slope of 30 mV decade^{-1}.

Next, voltammograms were simulated with the ΔpK_a value in the plateau region ($-2 > \Delta pK_a \geq -8$), but with k_{PT} values extrapolated from the LFER region (assuming a theoretical Brønsted slope of 0.5 that extends across the entire ΔpK_a range) until the diffusion-limited rate constant of ~1×10^{10} M^{-1} s^{-1} is reached. The diffusion limit for these complexes in this solvent system was previously estimated using the Debye–Smoluchowski equation.[9] In these simulated voltammograms, $E_{p,c}$ varies with scan rate, as anticipated for an EC reaction (Figure S69) and observed experimentally. However, in contrast to the simulations performed in the LFER region ($8 \geq \Delta pK_a \geq -2$), the observed $E_{p,c}$ of the Co(II/I) reduction feature in the simulations do not vary as a function of the k_{PT} values input (Figure 3), such that k_{PT}^{app} is independent of the input k_{PT} values (and thus ΔpK_a). Peak shift analysis (eq 4) of the $E_{p,c}$ values from the simulated voltammograms yields k_{PT}^{app} = 9×10^6 M^{-1} s^{-1} (for theoretical k_{PT} input values 10^8 M^{-1} s^{-1} $\leq$ k_{PT} $\leq$ 10^{10} M^{-1} s^{-1}). The discrepancies between k_{PT}^{app} and the input k_{PT} indicate that in the plateau region the apparent proton transfer rate constants are not a direct measurement of the elementary proton transfer step. Surface concentration profiles for these simulations explain this finding, showing that with large intrinsic k_{PT} values, k_{PT}^{app} values are dictated by the parameters that describe both ligand dissociation from [CoCp(dppe)(NCCH$_3$)]$^+$ and protonation of CoCp(dppe) (Figure S72, Supporting Information).

Upon varying the acid concentration (0.3–100 mM) at a fixed scan rate (200 mV s^{-1}) with k_{PT} = 1×10^9 M^{-1} s^{-1}, the evolution of $E_{p,c}$ for the Co(II/I) feature shows intriguing behavior in the simulated voltammograms (Figure 4). For acid concentrations < 20 mM, the $E_{p,c}$ shifts to more positive potentials with increasing acid concentration, varying linearly with log([HA]) with the slope of ~30 mV decade^{-1} as predicted by eq 4 for a canonical EC reaction (Figure 4). By contrast, $E_{p,c}$ becomes independent of acid concentration when it exceeds 20 mM, implicating a change in the rate law. To verify this behavior experimentally, we collected voltammograms of 0.5 mM **1** recorded in CH$_3$CN with high concentrations of anilinium (pK_a = 10.41); indeed $E_{p,c}$(Co(II/I)) becomes invariant with acid concentrations > 30 mM (Figure S70).

A simulated Brønsted plot was constructed from the apparent rate constants (k_{PT}^{app}) obtained from the $E_{p,c}$ values of voltammograms simulated using the reaction mechanism described in Scheme 4 for the reaction of **1** with acids spanning a ΔpK_a range of 16 units ($8 \geq \Delta pK_a \geq -8$) in CH$_3$CN. This plot exhibits a plateau in k_{PT}^{app} values for exergonic proton transfer reactions ($k_{plateau} \approx 8.5 \times 10^6$ M^{-1} s^{-1}) and a Brønsted slope of α = 0.42 in the LFER region (Figure 5). This simulated Brønsted plot is in qualitative agreement with the experimental plot (Figure 3, $k_{plateau} \approx 1.7 \times 10^7$ M^{-1} s^{-1}; α_1 = 0.55); differences are attributed to the approximated k_d and K_{eq} values used for the simulations. These simulations suggest that dissociation of CH$_3$CN from [CoCp(dppe)(NCCH$_3$)]$^+$ gates protonation of CoCp(dppe), leading to the observed plateau of k_{PT}^{app} values with stronger acids. To evaluate this further, Brønsted plots were simulated as a function of both k_d and K_{eq} values. Varying k_d from 10^3 to 10^{14} s^{-1} led to no changes in the calculated k_{PT}^{app} values. However, K_{eq} influences the absolute values of k_{PT}^{app} in both the LFER and plateau regions of the

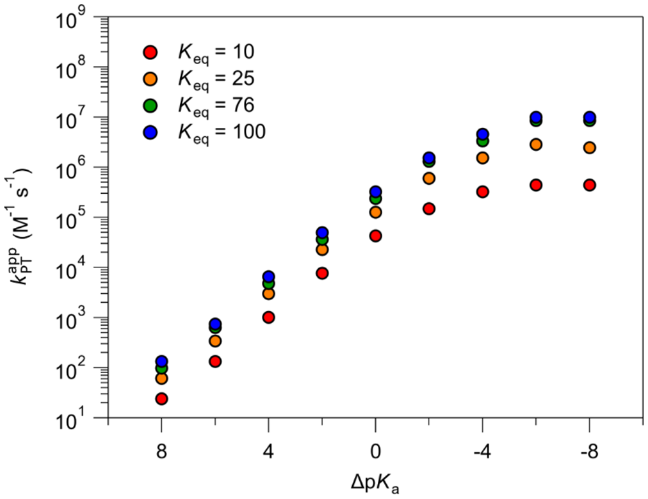

Figure 5. Simulated Brønsted plots as a function of K_{eq} for CH$_3$CN dissociation from [CoCp(dppe)(NCCH$_3$)]$^+$.

Brønsted plot; higher K_{eq} values correspond to higher values of $k_{\mathrm{PT}}^{\mathrm{app}}$, with differences most pronounced in the plateau region (Figure 5). With K_{eq} = 10 M, k_{plateau} is ∼4×10^5 M^{-1} s^{-1}; a 10-fold increase in K_{eq} increases k_{plateau} by nearly 2 orders of magnitude (∼1×10^7 M^{-1} s^{-1}). The observation that K_{eq}, but not k_d, influences $k_{\mathrm{PT}}^{\mathrm{app}}$ indicates that the thermodynamics (and not kinetics) of this acetonitrile dissociation $[\mathrm{CoCp(dppe)(NCCH_3)}]^+$ dictate the observed kinetics of CoCp(dppe) protonation. Owing to the complex kinetics described by Scheme 4, involving multiple competing chemical and electrochemical reactions, we refrain from deriving a quantitative rate law to describe this reaction. Nevertheless, these comprehensive kinetics simulations support the conclusion that the observed plateau in $k_{\mathrm{PT}}^{\mathrm{app}}$ values with stronger acids reflects gating of CoCp(dppe) generation (and its subsequent protonation) by CH_3CN dissociation from $[\mathrm{CoCp(dppe)(NCCH_3)}]^+$.

Protonation Kinetics in Noncoordinating Solvents in the Plateau Region. As detailed above, the equilibrium constant for the CH_3CN dissociation (K_{eq}) from $[\mathrm{CoCp(dppe)(NCCH_3)}]^+$ is solvent dependent. On the basis of the strong interdependence between the k_{plateau} and K_{eq} in the simulated Brønsted plots (Figure 5), we hypothesized that experimental Brønsted plots recorded in different solvents would enable us to support the conclusion that the $k_{\mathrm{PT}}^{\mathrm{app}}$, and the associated k_{plateau} values, are dictated by K_{eq}. $k_{\mathrm{PT}}^{\mathrm{app}}$ values for **1** with three acids in the plateau region (4-CF_3-2,3,5,6-tetrafluorophenol, *p*-toluenesulfonic acid, and dimethylformamidinium triflate, Tables S4 and S5) were determined from voltammograms recorded as a function of scan rate and acid concentration in both DFB and CH_2Cl_2. The selection of acids was dictated by common solubility of acids in these two solvents. As in CH_3CN, the Co(II/I) couple becomes irreversible in DFB and CH_2Cl_2 upon addition of acid and the peak potential shifts as a function of acid concentration and scan rate, enabling ready determination of the apparent $k_{\mathrm{PT}}^{\mathrm{app}}$ via eq 4. Notably, $E_{\mathrm{p,c}}$ becomes insensitive to acid concentration at higher acid concentrations, as observed in CH_3CN. For instance, with a 1 mM solution of **1** in DFB, the $E_{\mathrm{p,c}}$ stops changing when the concentration of 4-CF_3-2,3,5,6-tetrafluorophenol exceeds 50 mM (Figure S71).

Comparison of $k_{\mathrm{PT}}^{\mathrm{app}}$ values for **1** in DFB and CH_2Cl_2 in the plateau region (Figure 6) reveals that the observed plateau rate constant (k_{plateau}) in DFB (6×10^5 $M^{-1}s^{-1}$) is ∼7 times lower than that in CH_2Cl_2 (4×10^6 M^{-1} s^{-1}). This aligns with the differences in experimentally determined K_{eq} values for these solvents (K_{eq} = 76 M in CH_2Cl_2, 25 M in DFB), supporting the conclusions that $k_{\mathrm{PT}}^{\mathrm{app}}$ is influenced by CH_3CN dissociation from the electrochemically generated Co(II) species. Of note, $k_{\mathrm{PT}}^{\mathrm{app}}$ values for weaker acids (acetic acid, 2,3,4,6-tetrafluorophenol, and salicylic acid) determined in DFB indicate an LFER region is accessible, similar to CH_3CN data (Figure 6, Table S5).

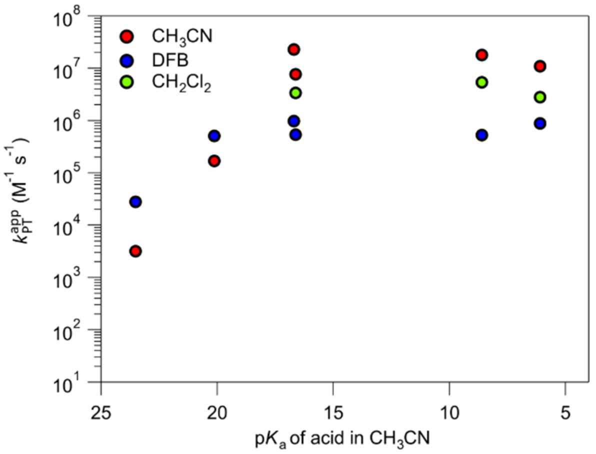

Figure 6. $k_{\mathrm{PT}}^{\mathrm{app}}$ values for the protonation of CoCp(dppe) with selected acids in CH_3CN, CH_2Cl_2, and DFB, plotted as a function of acid pK_a in CH_3CN.

Returning to the observation that the k_{plateau} values for **1**, **2**, and **3** span nearly 3 orders of magnitude in CH_3CN, we hypothesized that the differences in chelating phosphine ligands influence the K_{eq} values for acetonitrile dissociation from the corresponding $[\mathrm{CoCp(dxpe)(NCCH_3)}]^+$ species, and this in turn gives rise to the dramatic differences in k_{plateau} values. Because K_{eq} values are not tractable in neat CH_3CN, we compared $k_{\mathrm{PT}}^{\mathrm{app}}$ values for **1** and **2** in DFB with three acids expected to fall in the plateau region (4-CF_3-2,3,5,6-tetrafluorophenol, *p*-toluenesulfonic acid, and dimethylformamidium triflate; Tables S4 and S6). Indeed, $k_{\mathrm{PT}}^{\mathrm{app}}$ values were independent of acid strength for these strong acids for both **1** and **2**, and from these data k_{plateau} values were determined (Figure 7). The ratio of $k_{\mathrm{plateau\text{-}2}}/k_{\mathrm{plateau\text{-}1}}$ ≈ 3.3 in DFB ($k_{\mathrm{plateau\text{-}2}} = 2 \times 10^6$ M^{-1} s^{-1}, $k_{\mathrm{plateau\text{-}1}} = 6 \times 10^5$ M^{-1} s^{-1}), in qualitative agreement with their relative K_{eq} values in DFB ($K_{\mathrm{eq\text{-}2}}$ = 50 M, $K_{\mathrm{eq\text{-}1}}$ = 25 M). Collectively, these data indicate that the steric profile of the chelating phosphine ligands impacts the K_{eq} for CH_3CN dissociation.

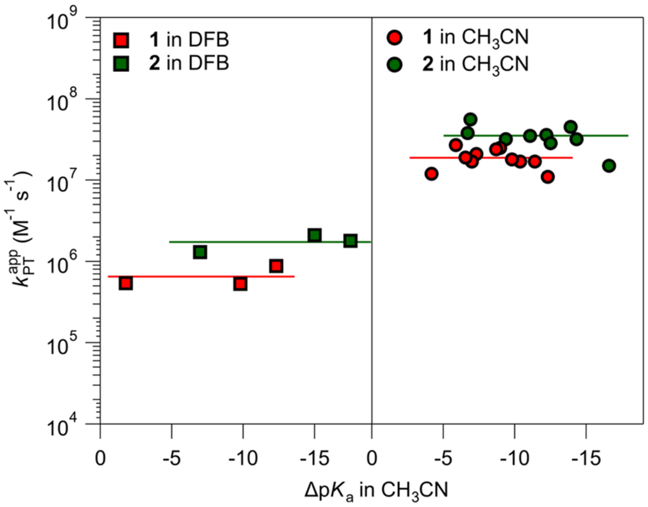

Figure 7. Side-by-side comparison of Brønsted plots for complexes **1** and **2** (left) in DFB with 3 acids in the plateau region (4-CF_3-2,3,5,6-tetrafluorophenol, *p*-toluenesulfonic acid, and dimethylformamidium triflate) and (right) in CH_3CN with all the plateau region acids shown in Figure 2.

The observation that the bulkier dppe ligand of **1** corresponds to a lower propensity (smaller K_{eq}) for ligand dissociation than the less bulky depe ligand of **2** initially seems counterintuitive. However, recognizing that structural reorganization associated with ligand dissociation (which involves the dxpe ligands moving into the Cp−Co plane) should influence the equilibrium described by K_{eq}, a smaller barrier for geometric reorganization should correspond to a larger K_{eq}. Taking the self-exchange rate constants for **1** and **2** ($k_{\mathrm{self\text{-}1}}$ = 3.1

M^{-1} s^{-1}; $k_{self\text{-}2}$ = 61 M^{-1} s^{-1}; see above) as a proxy for geometric reorganization energies, the observed trends between K_{eq} and ligand sterics are readily justified. While neither K_{eq} nor $k_{self\text{-}3}$ was experimentally accessible for the dcpe complex **3**, we predict that the steric bulk of the cyclohexyl substituents will lead to a $k_{self\text{-}3}$ that is substantially smaller than $k_{self\text{-}1}$ and $k_{self\text{-}2}$, and in turn a smaller K_{eq}. Thus, the observed differences in k_{PT}^{app} for **1**, **2**, and **3** across both the LFER and plateau regions are best described by differences in the relative K_{eq} values, which are dictated by the geometric reorganization accompanying CH_3CN dissociation, such that less bulky ligands have larger $k_{plateau}$ values.

Together, observed trends between k_{PT}^{app} and ligand sterics; successful digital simulation of experimental voltammograms as a function of acid concentration, scan rate, k_{PT}, and K_{eq}; correlation between K_{eq} and $k_{plateau}$ values as a function of both solvent and ligand sterics; and deuterium exchange reactions support the conclusion that the proton-coupled electron transfer reaction to generate $[HCoCp(dxpe)]^+$ is well-described by the multistep reaction depicted in Scheme 4. In this mechanism, a bound acetonitrile must dissociate from the electrochemically generated $[CoCp(dxpe)(NCCH_3)]^+$ species before undergoing subsequent reduction and protonation. Further, the initial protonation occurs at the Cp ligand, followed by an intramolecular proton transfer to form the product $[HCoCp(dxpe)]^+$. Crucially, these data support the conclusion that CH_3CN dissociation from $[CoCp(dxpe)(NCCH_3)]^+$ gates the proton transfer to CoCp(dxpe) when the intermolecular proton transfer rate constants are very fast, leading to a plateau in k_{PT}^{app} with stronger acids. In the LFER region, the k_{PT}^{app} values determined are reflective of the intrinsic rate constant for protonation of CoCp(dxpe) (k_{PT}), but as k_{PT} becomes larger, k_{PT}^{app} is dictated by the K_{eq} for CH_3CN dissociation (supported by correlations between $k_{plateau}$ and K_{eq} values as a function of ligand and solvent) and k_{PT} (supported by the acid concentration influence on $E_{p,c}$, which gives rise to second-order k_{PT}^{app} values at low to moderate acid concentrations). At very high acid concentrations, k_{PT}^{app} becomes acid-independent and is solely dictated by K_{eq}.

CONCLUSIONS

A series of Co(III) complexes with the general formula $[CoCp(dxpe)(NCCH_3)]^{2+}$ (**1**−**3**) were prepared with a series of phosphine ligands with substituents that vary in their steric bulk (ethyl, phenyl, and cyclohexyl). Two-electron, one-proton PCET reactivity of these complexes leads to the formation of the corresponding hydride species $[HCoCp(dxpe)]^+$. Through cyclic voltammetry measurements recorded in the presence of molecular acids of varying strength, reactivity was determined to proceed via two-electron reduction of the Co(III) precursors followed by protonation to form the corresponding HCo(III) complexes. From electrochemical peak shift analysis of the Co(II/I) reduction step, k_{PT}^{app} values were determined for each complex. Brønsted plots correlating k_{PT}^{app} vs ΔpK_a show stark differences based on the steric bulk of the phosphine ligand: the ethyl-substituted complex **2** has higher k_{PT}^{app} values in comparison to the phenyl-substituted complex **1**, and the bulky cyclohexyl-substituted complex **3** has much lower k_{PT}^{app} values. For all complexes, k_{PT}^{app} vs ΔpK_a exhibited a linear free-energy relationship for endergonic to mildly exergonic protonation reactions (when $\Delta pK_a > -2$), and k_{PT}^{app} values plateaued for protonation reactions with larger driving forces at values well below the diffusion limit for proton transfer. When proton sources with steric bulk around the acidic proton are utilized, k_{PT}^{app} is dramatically attenuated for all three complexes, with acid pK_a values spanning across both regions.

KIE experiments in the LFER region and the plateau region reveal that there is a different rate-limiting step in the two regimes, a curious finding for a seemingly simple proton transfer reaction. When deuterium-labeled acids were used to protonate isolated Co(I) complexes, deuterium incorporation into the Cp ring was observed, indicating CpH formation followed by tautomerization to form HCo(III). This indicates an intrinsic barrier to direct metal protonation, a finding that has ramifications on the design of catalysts for fuel production that proceeds via metal hydride intermediates. However, the ligand-based protonation observed in this and other cyclopentadienyl−metal complexes suggests there may be opportunities to exploit metal−ligand cooperativity to overcome these intrinsic barriers through alternative reaction pathways, and future work in this area should examine these opportunities.

Digital simulations revealed further mechanistic nuances; dissociation of a bound CH_3CN upon reduction of Co(III) to Co(II) gates subsequent electron and proton transfer. When the PCET reaction is endergonic or mildly exergonic, k_{PT}^{app} reflects the intrinsic rate constant for protonation of Co(I). However, when the rate constant for protonation increases, the apparent kinetics of protonation are influenced by the equilibrium constant for ligand dissociation from Co(II) (described by K_{eq}). These mechanistic findings are supported by correlations between experimental K_{eq} and k_{PT}^{app} values in the plateau region as a function of both solvent and chelating phosphine ligand. These findings emphasize that seemingly simple proton-coupled electron transfer reactions may proceed via unexpected elementary reaction steps, and a detailed understanding of reaction mechanisms is critical to advance our understanding and the development of catalysts that mediate proton-coupled electron transfer processes.

EXPERIMENTAL METHODS

General Considerations. All experiments were performed in a nitrogen-filled glovebox, unless otherwise noted. All glovebox solvents were degassed with argon and dried using a Pure Process Technology solvent purification system. Tetrabutylammonium hexafluorophosphate (TCI, 98%) was recrystallized from ethanol. 1,2-Bis(diphenylphosphino)ethane (Ark Pharm, 97%), 1,2-bis(diethylphosphino)ethane (Sigma-Aldrich, 97%), 1,2-bis(dicyclohexylphosphino)ethane (Acros Organics, 98%), dimethyl sulfide (Sigma-Aldrich, anhydrous ≥ 99%), and cyclopentadienylcobalt dicarbonyl (Strem, >95%) were used as received. Acetonitrile-d_6 (99.8% D) and benzene-d_6 was purchased from Cambridge Isotope Laboratories.

^1H, $^{13}C\{^1H\}$, and $^{31}P\{^1H\}$ NMR spectra were collected on either a Bruker 600 or Bruker 500 MHz spectrometer at 295 K. 2D-EXSY NMR spectra were collected on a Bruker 700 MHz spectrometer at 295 K. Chemical shifts are reported relative to residual proteo solvent signals. UV−vis absorption spectra were collected using either an Agilent Cary 60 UV−vis absorbance spectrophotometer or an OceanOptics FLAME-S-UV−vis spectrometer with a DH-mini light source.

Samples were analyzed with a Q Exactive HF-X (ThermoFisher, Bremen, Germany) mass spectrometer. Samples were introduced via a heated electrospray source (HESI) at a flow rate of 10 μL/min. One hundred time domain transients were averaged in the mass spectrum. HESI source conditions were set as follows: nebulizer temperature 100 °C, sheath gas (nitrogen) 15 arb, auxiliary gas (nitrogen) 5 arb, sweep gas (nitrogen) 0 arb, capillary temperature 250 °C, RF voltage

100 V. The mass range was set to 600−2000 m/z. All measurements were recorded at a resolution setting of 120 000. Solutions were analyzed at 0.1 mg/mL or less based on responsiveness to the ESI mechanism. Xcalibur (ThermoFisher, Breman, Germany) was used to analyze the data. Molecular formula assignments were determined with Molecular Formula Calculator (v 1.2.3). All observed species were singly charged, as verified by unit m/z separation between mass spectral peaks corresponding to the ^{12}C and ^{13}C^{12}C$_{c\text{-}1}$ isotope for each elemental composition.

Sample Preparation for 2D EXSY Experiments. To a suspension/solution of [HCoCp(dxpe)][PF$_6$] in THF was added an excess of NaH (10−100 equivalents). The suspension was stirred overnight at room temperature in the glovebox, which was accompanied by a color change from yellow to red. The mixture was dried under vacuum and resuspended in toluene. The mixture was stirred overnight, followed by filtration to get rid of excess NaH, unreacted [HCoCp(dxpe)][PF$_6$], and NaPF$_6$. The filtrate was then dried under vacuum to afford CoCp(dxpe). This was then dissolved in the NMR solvent along with a known amount of [HCoCp(dxpe)][PF$_6$] solid and a known amount of diethyl ether as an internal standard.

Electrochemical Methods. Electrochemical measurements were performed using published procedures.[9] All measurements were performed in a N$_2$-filled glovebox with a WaveDriver (Pine Research) potentiostat using a 3 mm diameter carbon working electrode, a 3 mm diameter glassy carbon counter electrode, and a silver wire pseudo-reference electrode. A 20 mL scintillation vial was used as an electrochemical cell, fitted with a custom-made Teflon cap to hold the three electrodes. The electrode leads in the glovebox were connected to the potentiostat with a custom shielded electrode cable feed-through. All scans were referenced to the ferrocenium/ferrocene couple at 0 V. Acetonitrile (Fisher Scientific, HPLC grade, >99.9%) for electrochemical experiments was dried and degassed using a Pure Process Technology solvent purification system. Ferrocene was present in each scan unless otherwise noted. Ohmic drop was minimized using a high electrolyte concentration (0.25 M tetrabutylammonium hexafluorophosphate, [NBu$_4$][PF$_6$]), through minimization of the distance between the working and reference electrodes, and through manual iR compensation. Glassy carbon electrodes (CH Instruments, 3 mm diameter disk) were polished with 0.05 μm alumina powder (CH Instruments, contained no agglomerating agents) Milli-Q water slurries, rinsed, and ultrasonicated briefly in Milli-Q water to remove residual polishing powder. The silver wire pseudo-reference electrode was submerged in a glass tube containing electrolyte (0.25 M [NBu$_4$][PF$_6$] in acetonitrile, CH$_3$CN) and separated from the solution with a porous glass Vycor tip. The working electrode was pretreated with cyclical scans from approximately 2 to −2 V (the exact value varied in accordance with the silver wire pseudo-reference) at 250 mV s^{-1} in 0.25 M [NBu$_4$][PF$_6$] until cycles were superimposable (typically achieved within three cycles).

Digital Simulations. Digital simulations of cyclic voltammograms were performed with DigiElch 8.FD electrochemical simulation software (ElchSoft through Gamry Instruments). Simulation parameters are detailed in Scheme S1 (Supporting Information).

Computational Details. DFT calculations were performed with the ORCA program package, version 4.0.1.[44] Optimized geometries were computed using the BP86 functional.[45,46] Atom-pairwise dispersion correction with the Becke−Johnson damping scheme (D3BJ),[47,48] the scalar relativistic zero-order regular approximation (ZORA),[49] and the scalar relativistically recontracted version of the Aldrichs triple-ζ basis set, def2-TZVP, were used on all atoms with an auxiliary basis set of def2/J.[50] The conductor-like polarizable continuum model[51] (CPCMC) was used to simulate an acetonitrile solution (ε = 36.6). Resolution of identity (RI) was used to approximate two electron integrals for geometry optimizations and the numerical frequency calculations. The SCF calculations were tightly converged (TightSCF). Optimizations were tightly converged (TightOpt). Numerical integrations during all DFT calculations were done on a dense grid (ORCA grid4). The calculated structures were confirmed to be minima on the potential energy surface by the absence of imaginary frequencies after numerical frequency calculations on the optimized structures.

*Synthesis of [CoCp(depe)(NCCH$_3$)][PF$_6$]$_2$ (**2**).* To a stirring solution of [CoCp(SMe$_2$)$_3$][PF$_6$]$_2$ (202 mg, 0.34 mmol) in 5 mL of CH$_3$CN was added slowly depe (80 μL, 0.34 mmol) with an accompanying color change from pink to dark orange. The solution was stirred at 295 K for 48 h, filtered, and then evaporated to dryness. Dichloromethane (10 mL) was added to the residue, followed by sonication until a free-flowing powder was obtained. The powder was collected and redissolved in minimal CH$_3$CN, and the solution was added dropwise to stirred diethyl ether to obtain a bright orange powder. The orange powder was dried under reduced pressure and was obtained in 60% yield. ^{1}H NMR (600 MHz, CD$_3$CN): δ 5.71 (s, 5H), 2.45 (dp, J = 15.0, 7.4 Hz, 2H), 2.35−2.20 (m, 4H), 2.11−1.98 (m, 6H), 1.97 (s, 3H), 1.34 (dt, J = 19.0, 7.7 Hz, 6H), 1.27 (td, J = 16.4, 7.4 Hz, 6H). ^{13}C{^{1}H} NMR (151 MHz, CD$_3$CN): δ 137.29, 90.27, 21.87 (dd, J = 21.4, 18.3 Hz), 20.43 (dd, J = 15.6, 12.8 Hz), 17.88 (dd, J = 15.0, 12.2 Hz), 7.78, 4.59 (p, J = 21.4 Hz). ^{31}P{^{1}H} NMR (243 MHz, CD$_3$CN): δ 89.72 (2P), −145.00 (hept, J = 705.7 Hz, 2P). Anal. Calcd for $C_{17}H_{32}CoF_{12}NP_4$: C, 30.88; H, 4.88, N, 2.12. Found: C, 30.79; H, 4.98, N, 2.03.

*Synthesis of [CoCp(dcpe)(NCCH$_3$)][PF$_6$]$_2$ (**3**).* To a stirring solution of [CoCp(SMe$_2$)$_3$][PF$_6$]$_2$ (87.9 mg, 0.14 mmol) in 5 mL of CH$_3$CN was added dcpe (62 mg, 0.15 mmol) with an accompanying color change from pink to dark orange. The solution was stirred at 295 K overnight, after which is was filtered. The filtrate was added dropwise to diethyl ether, and the resulting solid was collected and dried via filtration. The solid was then suspended in chloroform, sonicated, filtered, and washed with chloroform, then dried under high vacuum to give **3** as an orange solid in 70% yield. ^{1}H NMR (600 MHz, CD$_3$CN): δ 5.88 (s, 5H), 2.26−2.11 (m, 4H), 2.07−1.98 (m, 4H), 1.96 (s, 3H), 1.93−1.85 (m, 14H), 1.79−1.50 (m, 10H), 1.46−1.29 (m, 16H). ^{13}C{^{1}H} NMR (151 MHz, CD$_3$CN): δ 139.53, 90.00, 40.96 (dd, J = 11.4, 9.3 Hz), 39.33 (dd, J = 11.5, 9.2 Hz), 30.22, 30.10 (td, J = 60.6, 2.7 Hz), 29.65, 28.05 (t, J = 6.1 Hz), 27.79 (t, J = 5.3 Hz), 27.64 (t, J = 5.4 Hz), 27.55 (t, J = 5.7 Hz), 26.05 (d, J = 33.0 Hz), 21.34 (dd, J = 19.4, 15.5 Hz). ^{31}P{^{1}H} NMR (243 MHz, CD$_3$CN): δ 92.49 (2P), −145.00 (hept, J = 705.7 Hz, 2P). Anal. Calcd for $C_{33}H_{56}CoF_{12}NP_4$: C, 45.16; H, 6.43, N, 1.60. Found: C, 45.80; H, 6.76, N, 0.48.

*Synthesis of [HCoCp(depe)][PF$_6$] (**5**).* CoCp(CO)$_2$ (0.25 mL, 1.87 mmol) and depe (0.44 mL, 1.88 mmol) were combined in 20 mL of toluene in a bomb flask. The bomb flask was put on the Schlenk line under an N$_2$ atmosphere and heated at 105 °C for 30 min, wherein the color changed from light red to dark red with bubbling for the first 10 min. After the reaction flask was cooled to room temperature, the bomb flask was brought back into the glovebox and the reaction mixture was diluted with 20 mL of methanol. Solid NH$_4$PF$_6$ (618 mg, 3.79 mmol) was added to the mixture, and it was stirred overnight, wherein the color changed from dark red to dark orange with a small amount of yellow precipitate. The entire mixture was then added to 200 mL of diethyl ether with vigorous stirring to yield a pale yellow powder. The yellow solid was filtered, rinsed with ether, and dried under high vacuum (79%). Vapor diffusion of diethyl ether into a concentrated solution of the solid in CH$_3$CN yielded large orange crystals of **5**. ^{1}H NMR (500 MHz, CD$_3$CN): δ 5.12 (s, 5H), 2.07 (ddt, J = 15.0, 10.2, 7.6 Hz, 2H), 1.99−1.90 (m, 5H), 1.88−1.76 (m, 4H), 1.74−1.57 (m, 2H), 1.12 (td, J = 16.3, 7.6 Hz, 6H), 1.07 (td, J = 18.2, 7.6 Hz, 6H), −16.73 (t, J = 69.7 Hz, 1H). ^{13}C{^{1}H} NMR (126 MHz, CD$_3$CN): δ 85.00, 24.68 − 24.44 (m), 24.35 (dd, J = 7.4, 3.9 Hz), 24.19 (d, J = 3.4 Hz), 8.80 (t, J = 1.4 Hz), 8.68 (t, J = 2.7 Hz). ^{31}P{^{1}H} NMR (202 MHz, CD$_3$CN): δ 95.58 (1P), −145.00 (hept, J = 706.5 Hz, 2P). HRMS: (HESI/Orbitrap) m/z [M − PF$_6$]$^+$ calcd for $C_{15}H_{30}P_2Co$ 331.11547; found 331.11472.

*Synthesis of [HCoCp(dcpe)][PF$_6$] (**6**).* CoCp(CO)$_2$ (0.23 mL, 1.72 mmol) and dcpe (0.704 mg, 1.67 mmol) were combined in 10 mL of toluene in a bomb flask. The bomb flask was put on the Schlenk line under an N$_2$ atmosphere and heated at 100 °C for 3 h, wherein the color changed from light red to dark red with bubbling for the first 10 min. After the flask was cooled to room temperature, it was brought back into the glovebox and NH_4PF_6 (0.285 mg, 1.75 mmol) was added to the toluene solution, followed by 10 mL of methanol. The suspension was stirred vigorously in the glovebox for 16 h, which resulted in the precipitation of a yellow solid. The pale yellow solid was filtered, rinsed with diethyl ether, and dried under high vacuum (74% yield). Vapor diffusion of diethyl ether into a concentrated solution of the solid in CH_3CN yielded orange crystals of **6**. ^{1}H NMR (500 MHz, CD_3CN): δ 5.20 (s, 5H), 2.08−1.96 (m, 6H), 1.94−1.76 (m, 14H), 1.76−1.68 (m, 4H), 1.56−1.44 (m, 4H), 1.43−1.23 (m, 20H), −16.54 (t, J = 69.8 Hz, 1H). ^{13}C{^{1}H} NMR (126 MHz, CD_3CN): δ 84.83, 38.85 (td, J = 18.1, 8.1 Hz), 37.01 (td, J = 18.5, 8.1 Hz), 29.52, 29.47, 29.04 (t, J = 2.4 Hz), 28.94, 27.72 (td, J = 12.6, 6.1 Hz), 27.21 (dt, J = 19.2, 5.9 Hz), 26.64 (d, J = 2.3 Hz), 22.62 (dd, J = 23.4, 17.0 Hz). ^{31}P{^{1}H} NMR (202 MHz, CD_3CN): δ 107.26, −145.00 (hept, J = 706.5 Hz). HRMS: (HESI/Orbitrap) m/z $[M - PF_6]^+$ calcd for $C_{31}H_{54}P_2Co$ 547.30327; found 547.30263.

■ ASSOCIATED CONTENT

Supporting Information

The Supporting Information is available free of charge at https://pubs.acs.org/doi/10.1021/jacs.0c11992.

Further experimental details, characterization data, additional experimental and simulated cyclic voltammograms (PDF)

Accession Codes

CCDC 2040905−2040906 contain the supplementary crystallographic data for this paper. These data can be obtained free of charge via www.ccdc.cam.ac.uk/data_request/cif, or by emailing data_request@ccdc.cam.ac.uk, or by contacting the Cambridge Crystallographic Data Centre, 12 Union Road, Cambridge CB2 1EZ, UK; fax: +44 1223 336033.

■ AUTHOR INFORMATION

Corresponding Author

Jillian L. Dempsey − *Department of Chemistry, University of North Carolina at Chapel Hill, Chapel Hill, North Carolina 27599-3290, United States*; orcid.org/0000-0002-9459-4166; Email: dempseyj@email.unc.edu

Authors

Daniel A. Kurtz − *Department of Chemistry, University of North Carolina at Chapel Hill, Chapel Hill, North Carolina 27599-3290, United States*; orcid.org/0000-0002-0082-1699

Debanjan Dhar − *Department of Chemistry, University of North Carolina at Chapel Hill, Chapel Hill, North Carolina 27599-3290, United States*

Noémie Elgrishi − *Department of Chemistry, University of North Carolina at Chapel Hill, Chapel Hill, North Carolina 27599-3290, United States; Department of Chemistry, Louisiana State University, Baton Rouge, Louisiana 70803, United States*; orcid.org/0000-0001-9776-5031

Banu Kandemir − *Department of Chemistry, University of North Carolina at Chapel Hill, Chapel Hill, North Carolina 27599-3290, United States*

Sean F. McWilliams − *Department of Chemistry, University of North Carolina at Chapel Hill, Chapel Hill, North Carolina 27599-3290, United States*

William C. Howland − *Department of Chemistry, University of North Carolina at Chapel Hill, Chapel Hill, North Carolina 27599-3290, United States*

Chun-Hsing Chen − *Department of Chemistry, University of North Carolina at Chapel Hill, Chapel Hill, North Carolina 27599-3290, United States*; orcid.org/0000-0003-0150-9557

Complete contact information is available at: https://pubs.acs.org/10.1021/jacs.0c11992

Author Contributions

All authors have given approval to the final version of the manuscript.

Notes

The authors declare no competing financial interest.

■ ACKNOWLEDGMENTS

This work was supported by the U.S. Department of Energy, Office of Science, Office of Basic Energy Sciences, under Award No. DE-SC0015303 and the University of North Carolina at Chapel Hill. J.L.D. acknowledges support from a Packard Fellowship in Science and Engineering. D.A.K. acknowledges the support of the Kenan Graduate Fellowship, and W.C.H. acknowledges the support of the Taylor Fellowship. We thank the University of North Carolina's Department of Chemistry NMR Core Laboratory for their use of their NMR spectrometers, supported by the National Science Foundation under Grant No. CHE-0922858. We thank the University of North Carolina's Department of Chemistry Mass Spectrometry Core Laboratory, especially Brandie Ehrmann, for their assistance with mass spectrometry analysis, supported by the National Science Foundation under Grant No. CHE-1726291. We thank the University of North Carolina Medical Biomolecular NMR Laboratory Core Facility for the use of their NMR spectrometer, supported by the National Cancer Institute of the National Institutes of Health under Award No. P30CA016086. The content is solely the responsibility of the authors and does not necessarily represent the official views of the National Institutes of Health. We thank Shannon Stahl, Clark Landis, James Gerkin, and Alexander Miller for insightful discussions.

■ REFERENCES

(1) Dempsey, J. L.; Brunschwig, B. S.; Winkler, J. R.; Gray, H. B. Hydrogen Evolution Catalyzed by Cobaloximes. *Acc. Chem. Res.* **2009**, *42* (12), 1995−2004.

(2) Helm, M. L.; Stewart, M. P.; Bullock, R. M.; DuBois, M. R.; DuBois, D. L. A Synthetic Nickel Electrocatalyst with a Turnover Frequency Above 100,000 s^{-1} for H_2 Production. *Science* **2011**, *333* (6044), 863−866.

(3) Bediako, D. K.; Solis, B. H.; Dogutan, D. K.; Roubelakis, M. M.; Maher, A. G.; Lee, C. H.; Chambers, M. B.; Hammes-Schiffer, S.; Nocera, D. G. Role of Pendant Proton Relays and Proton-Coupled Electron Transfer on the Hydrogen Evolution Reaction by Nickel Hangman Porphyrins. *Proc. Natl. Acad. Sci. U. S. A.* **2014**, *111* (42), 15001−15006.

(4) Dempsey, J. L. Proton-Coupled Electron Transfer: Metal Hydrides Find the Sweet Spot. *Nat. Chem.* **2015**, *7* (2), 101−102.

(5) Connor, G. P.; Mayer, K. J.; Tribble, C. S.; McNamara, W. R. Hydrogen Evolution Catalyzed by an Iron Polypyridyl Complex in Aqueous Solutions. *Inorg. Chem.* **2014**, *53* (11), 5408−5410.

(6) Lewandowska-Andralojc, A.; Baine, T.; Zhao, X.; Muckerman, J. T.; Fujita, E.; Polyansky, D. E. Mechanistic Studies of Hydrogen Evolution in Aqueous Solution Catalyzed by a Tertpyridine-Amine Cobalt Complex. *Inorg. Chem.* **2015**, *54* (9), 4310−4321.

(7) Elgrishi, N.; Rountree, K. J.; McCarthy, B. D.; Rountree, E. S.; Eisenhart, T. T.; Dempsey, J. L. A Practical Beginner's Guide to Cyclic Voltammetry. *J. Chem. Educ.* **2018**, *95* (2), 197−206.

(8) Elgrishi, N.; McCarthy, B. D.; Rountree, E. S.; Dempsey, J. L. Reaction Pathways of Hydrogen-Evolving Electrocatalysts: Electrochemical and Spectroscopic Studies of Proton-Coupled Electron Transfer Processes. *ACS Catal.* **2016**, *6* (6), 3644−3659.

(9) Elgrishi, N.; Kurtz, D. A.; Dempsey, J. L. Reaction Parameters Influencing Cobalt Hydride Formation Kinetics: Implications for Benchmarking H_2-Evolution Catalysts. *J. Am. Chem. Soc.* **2017**, *139* (1), 239−244.

(10) Johnson, F. P. A.; George, M. W.; Hartl, F.; Turner, J. J. Electrocatalytic Reduction of CO_2 Using the Complexes $[Re(Bpy)(CO)_3L]^n$ (n = + 1, L = $P(OEt)_3$, CH_3CN; n = 0, L = Cl^-,Otf^- ; Bpy = 2,2′-Bipyridine; Otf^- = CF_3SO_3) as Catalyst Precursors: Infrared Spectroelectrochemical Investigation. *Organometallics* **1996**, *7333* (9), 3374−3387.

(11) Barrios-Landeros, F.; Carrow, B. P.; Hartwig, J. F. Effect of Ligand Steric Properties and Halide Identity on the Mechanism for Oxidative Addition of Haloarenes to Trialkylphosphine Pd(0) Complexes. *J. Am. Chem. Soc.* **2009**, *131* (23), 8141−8154.

(12) McMullin, C. L.; Fey, N.; Harvey, J. N. Computed Ligand Effects on the Oxidative Addition of Phenyl Halides to Phosphine Supported Palladium(0) Catalysts. *Dalt. Trans.* **2014**, *43* (36), 13545−13556.

(13) Zaccaria, F.; Cipullo, R.; Budzelaar, P. H. M.; Busico, V.; Ehm, C. Backbone Rearrangement during Olefin Capture as the Rate Limiting Step in Molecular Olefin Polymerization Catalysis and Its Effect on Comonomer Affinity. *J. Polym. Sci., Part A: Polym. Chem.* **2017**, *55* (17), 2807−2814.

(14) Chalkley, M. J.; Oyala, P. H.; Peters, J. C. Cp* Noninnocence Leads to a Remarkably Weak C-H Bond via Metallocene Protonation. *J. Am. Chem. Soc.* **2019**, *141* (11), 4721−4729.

(15) Chalkley, M. J.; Del Castillo, T. J.; Matson, B. D.; Peters, J. C. Fe-Mediated Nitrogen Fixation with a Metallocene Mediator: Exploring pK_a Effects and Demonstrating Electrocatalysis. *J. Am. Chem. Soc.* **2018**, *140* (19), 6122−6129.

(16) Chalkley, M. J.; Del Castillo, T. J.; Matson, B. D.; Roddy, J. P.; Peters, J. C. Catalytic N_2 -to-NH_3 Conversion by Fe at Lower Driving Force: A Proposed Role for Metallocene-Mediated PCET. *ACS Cent. Sci.* **2017**, *3* (3), 217−223.

(17) Pitman, C. L.; Finster, O. N. L.; Miller, A. J. M. Cyclopentadiene-Mediated Hydride Transfer from Rhodium Complexes. *Chem. Commun.* **2016**, *52* (58), 9105−9108.

(18) Johnson, S. I.; Gray, H. B.; Blakemore, J. D.; Goddard, W. A. Role of Ligand Protonation in Dihydrogen Evolution from a Pentamethylcyclopentadienyl Rhodium Catalyst. *Inorg. Chem.* **2017**, *56* (18), 11375−11386.

(19) Jung, S.; McCrory, C. C. L.; Ferrer, I. M.; Peters, J. C.; Jaramillo, T. F. Benchmarking Nanoparticulate Metal Oxide Electrocatalysts for the Alkaline Water Oxidation Reaction. *J. Mater. Chem. A* **2016**, *4* (8), 3068−3076.

(20) Schild, D. J.; Drover, M. W.; Oyala, P. H.; Peters, J. C. Generating Potent C-H PCET Donors: Ligand-Induced Fe-to-Ring Proton Migration from a Cp^*Fe^{III}-H Complex Demonstrates a Promising Strategy. *J. Am. Chem. Soc.* **2020**, *144* (44), 18963−18970.

(21) Quintana, L. M. A.; Johnson, S. I.; Corona, S. L.; Villatoro, W.; Goddard, W. A.; Takase, M. K.; VanderVelde, D. G.; Winkler, J. R.; Gray, H. B.; Blakemore, J. D. Proton-Hydride Tautomerism in Hydrogen Evolution Catalysis. *Proc. Natl. Acad. Sci. U. S. A.* **2016**, *113* (23), 6409.

(22) Hopkins, J. A.; Lionetti, D.; Day, V. W.; Blakemore, J. D. Chemical and Electrochemical Properties of [Cp*Rh] Complexes Supported by a Hybrid Phosphine-Imine Ligand. *Organometallics* **2019**, *38* (6), 1300−1310.

(23) Boyd, E. A.; Lionetti, D.; Henke, W. C.; Day, V. W.; Blakemore, J. D. Preparation, Characterization, and Electrochemical Activation of a Model [Cp*Rh] Hydride. *Inorg. Chem.* **2019**, *58* (6), 3606−3615.

(24) Lionetti, D.; Day, V. W.; Blakemore, J. D. Structural and Chemical Properties of Half-Sandwich Rhodium Complexes Supported by the Bis(2-Pyridyl)Methane Ligand. *Dalt. Trans.* **2019**, *48* (33), 12396−12406.

(25) Weberg, R. T.; Norton, J. R. Kinetic and Thermodynamic Acidity of Hydrido Transition-Metal Complexes. 6. Interstitial Hydrides. *J. Am. Chem. Soc.* **1990**, *112* (3), 1105−1108.

(26) Walker, H. W.; Kresge, C. T.; Ford, P. C.; Pearson, R. G. Rates of Deprotonation and pK_a Values of Transition Metal Carbonyl Hydrides. *J. Am. Chem. Soc.* **1979**, *101* (24), 7428−7429.

(27) Kresge, A. J. What Makes Proton Transfer Fast. *Acc. Chem. Res.* **1975**, *8* (10), 354−360.

(28) Kramarz, K. W.; Norton, J. R. Slow Proton-Transfer Reactions in Organometallic and Bioinorganic Chemistry. *Progress in Inorganic Chemistry* **2007**, *42*, 1−65.

(29) Edidin, R. T.; Sullivan, J. M.; Norton, J. R. Kinetic and Thermodynamic Acidity of Hydrido Transition-Metal Complexes. 4. Kinetic Acidities toward Aniline and Their Use in Identifying Proton-Transfer Mechanisms. *J. Am. Chem. Soc.* **1987**, *109* (13), 3945−3953.

(30) Kuhn, N.; Winter, M. Synthese Und Reaktivität von Dienylmetall-Verbindungen IV. Verbindungen Des Typs $C_5H_5Ni(R_2PX)X$. *J. Organomet. Chem.* **1982**, *232* (1), C48−C50.

(31) Harris, R. K.; Hodgkinson, P.; Pickard, C. J.; Yates, J. R.; Zorin, V. Chemical Shift Computations on a Crystallographic Basis: Some Reflections and Comments. *Magn. Reson. Chem.* **2007**, *45* (S1), S174−S186.

(32) Ciancanelli, R.; Noll, B. C.; DuBois, D. L.; DuBois, M. R. Comprehensive Thermodynamic Characterization of the Metal-Hydrogen Bond in a Series of Cobalt-Hydride Complexes. *J. Am. Chem. Soc.* **2002**, *124* (12), 2984−2992.

(33) Berning, D. E.; Miedaner, A.; Curtis, C. J.; Noll, B. C.; Rakowski DuBois, M. C.; DuBois, D. L. Free-Energy Relationships between the Proton and Hydride Donor Abilities of $[HNi(Diphosphine)_2]^+$ Complexes and the Half-Wave Potentials of Their Conjugate Bases. *Organometallics* **2001**, *20* (9), 1832−1839.

(34) Savéant, J.-M. *Elements of Molecular and Biomolecular Electrochemistry*; John Wiley & Sons, Inc.: Hoboken, NJ, USA, 2006.

(35) Sampson, M. D.; Nguyen, A. D.; Grice, K. A.; Moore, C. E.; Rheingold, A. L.; Kubiak, C. P. Manganese Catalysts with Bulky Bipyridine Ligands for the Electrocatalytic Reduction of Carbon Dioxide: Eliminating Dimerization and Altering Catalysis. *J. Am. Chem. Soc.* **2014**, *136* (14), 5460−5471.

(36) Fujita, E.; Creutz, C.; Sutin, N.; Szalda, D. J. Carbon Dioxide Activation by Cobalt(I) Macrocycles: Factors Affecting Carbon Dioxide and Carbon Monoxide Binding. *J. Am. Chem. Soc.* **1991**, *113* (1), 343−353.

(37) Mock, M. T.; Potter, R. G.; O'Hagan, M. J.; Camaioni, D. M.; Doughtery, W. G.; Kassell, W. S.; DuBois, D. L. Synthesis and Hydride Transfer Reactions of Cobalt and Nickel Hydride Complexes to BX_3 Compounds. *Inorg. Chem.* **2011**, *50* (23), 11914−11928.

(38) Kristjansdottir, S. S.; Loendorf, A. J.; Norton, J. R. Kinetic and Thermodynamic Acidity of Hydrido Transition-Metal Complexes. 9. A Sterically Hindered Cationic Hydride, $[H_4Re(PMe_2Ph)_4]^+$. *Inorg. Chem.* **1991**, *30* (23), 4470−4471.

(39) Jordan, R. F.; Norton, J. R. Kinetic and Thermodynamic Acidity of Hydrido Transition-Metal Complexes. 1. Periodic Trends in Group VI Complexes and Substituent Effects in Osmium Complexes. *J. Am. Chem. Soc.* **1982**, *104* (5), 1255−1263.

(40) Jordan, R. F.; Norton, J. R. Proton Transfer Reactions in Organometallic Chemistry. *ACS Symp. Ser.* **1982**, *Ch. 17*, 403−423, DOI: 10.1021/bk-1982-0198.ch017.

(41) Nikitin, K.; O'Gara, R. Mechanisms and Beyond: Elucidation of Fluxional Dynamics by Exchange NMR Spectroscopy. *Chem. - Eur. J.* **2019**, *25*, 1−40.

(42) Huang, T.; Rountree, E. S.; Traywick, A. P.; Bayoumi, M.; Dempsey, J. L. Switching between Stepwise and Concerted Proton-Coupled Electron Transfer Pathways in Tungsten Hydride Activation. *J. Am. Chem. Soc.* **2018**, *140* (44), 14655−14669.

(43) Churchill, D. G.; Janak, K. E.; Wittenberg, J. S.; Parkin, G. Normal and Inverse Primary Kinetic Deuterium Isotope Effects for C-H Bond Reductive Elimination and Oxidative Addition Reactions of Molybdenocene and Tungstenocene Complexes: Evidence for

Benzene σ-Complex Intermediates. *J. Am. Chem. Soc.* **2003**, *125* (5), 1403−1420.

(44) Neese, F. The ORCA Program System. *Wiley Interdiscip. Rev.: Comput. Mol. Sci.* **2012**, *2* (1), 73−78.

(45) Becke, A. D. Density Functional Calculations of Molecular Bond Energies. *J. Chem. Phys.* **1986**, *84* (8), 4524−4529.

(46) Perdew, J. P. Density-Functional Approximation for the Correlation Energy of the Inhomogeneous Electron Gas. *Phys. Rev. B: Condens. Matter Mater. Phys.* **1986**, *33* (12), 8822−8824.

(47) Grimme, S.; Antony, J.; Ehrlich, S.; Krieg, H. A Consistent and Accurate Ab Initio Parametrization of Density Functional Dispersion Correction (DFT-D) for the 94 Elements H-Pu. *J. Chem. Phys.* **2010**, *132* (15), 154104.

(48) Grimme, S.; Ehrlich, S.; Goerigk, L. Effect of the Damping Function in Dispersion Corrected Density Functional Theory. *J. Comput. Chem.* **2011**, *32* (7), 1456−1465.

(49) van Wüllen, C. Molecular Density Functional Calculations in the Regular Relativistic Approximation: Method, Application to Coinage Metal Diatomics, Hydrides, Fluorides and Chlorides, and Comparison with First-Order Relativistic Calculations. *J. Chem. Phys.* **1998**, *109* (2), 392−399.

(50) Weigend, F. Accurate Coulomb-Fitting Basis Sets for H to Rn. *Phys. Chem. Chem. Phys.* **2006**, *8* (9), 1057.

(51) Klamt, A.; Schüürmann, G. COSMO: A New Approach to Dielectric Screening in Solvents with Explicit Expressions for the Screening Energy and Its Gradient. *J. Chem. Soc., Perkin Trans. 2* **1993**, No. 5, 799−805.